Numerical and Experimental Investigation of the Flow-Induced Noise of a Wall-Mounted Airfoil

Paul Croaker, Danielle Moreau, Manuj Awasthi, Mahmoud Karimi, Con Doolan and Nicole Kessissoglou

Abstract A numerical and experimental investigation into the flow field around a finite wall-mounted airfoil is presented. Measurements were performed in an open-jet anechoic wind tunnel for a finite wall-mounted NACA 0012 airfoil with an aspect ratio of one. The airfoil was tested at zero degree angle of attack, with a Mach number of 0.06 and Reynolds number based on chord of 274,000. The measurements include single hotwire anemometry in the near-wake of the airfoil at a number of locations in the mid-span and tip regions. A large eddy simulation (LES) of flow past the airfoil was performed, and good agreement with measurements was obtained. Based on Lighthill's acoustic analogy, flow-induced noise sources were then extracted from the LES data. Sound radiation to the far-field and the incident acoustic pressure on the airfoil were both predicted using a near-field formulation for the aeroacoustic pressure. The boundary element method (BEM) was then used to predict the scattering of the incident pressure field by the airfoil as well as the total far-field acoustic pressure.

Keywords Computational fluid dynamics · Aeroacoustics · Wall-mounted foils Experimental measurements

1 Introduction

The sound produced by flow over finite wall-mounted airfoils is of practical interest in the design of quiet aircraft and marine vessels. Many of the lifting and control surfaces on these structures, such as the tailplane of an aircraft or a ship's rudder, can be approximated as wall-mounted airfoils. The flow past a finite wall-mounted airfoil is characterised by complex three-dimensional flow features. Vortex structures form at the airfoil tip which grow as they travel downstream and exert a strong influence on the flow over the airfoil in the near-tip region [4]. In the mid-span of the airfoil, a turbulent boundary layer develops and turbulent eddies are convected downstream

P. Croaker (✉) · D. Moreau · M. Awasthi · M. Karimi · C. Doolan · N. Kessissoglou
The University of New South Wales, UNSW Sydney, Sydney, NSW 2052, Australia
e-mail: p.croaker@unsw.edu.au

E. Ciappi et al. (eds.), *Flinovia—Flow Induced Noise and Vibration Issues and Aspects-II*,
https://doi.org/10.1007/978-3-319-76780-2_7

and past the trailing edge. For a blunt trailing edge, vortex shedding will also occur in the mid-span region. In the boundary layer of the wall, a horseshoe vortex forms around the base of the airfoil starting at the leading edge and extending into the wake [3, 9]. For low Mach number flows, the nature and strengths of these flow structures vary with Reynolds number, airfoil section and aspect ratio as well as the incoming wall boundary layer thickness [10]. Due to the complex flow over a wall-mounted airfoil, a number of different flow-induced noise mechanisms occur. Interaction between the flow structures in the turbulent boundary layer of the wall and the airfoil leading edge produces low-frequency noise. Convection of turbulent eddies past the trailing edge as well as vortex shedding from the blunt trailing edge contributes to broadband noise. Further, the interaction between the tip vortices and the trailing edge of the airfoil tip can produce strong broadband noise peaks at higher frequencies [7].

This paper presents numerical prediction and measurements of the flow field around a finite wall-mounted NACA 0012 airfoil with an aspect ratio of one at a Reynolds number based on chord Re_c = 274,000 and zero degree angle of attack. Mean and root-mean-square (rms) velocity profiles as well as velocity spectra are measured using hotwire anemometry in the near-wake of the airfoil in the mid-span and tip regions. These measurements are used to validate the numerical prediction of the hydrodynamic field obtained using an LES model. The hybrid CFD-BEM technique of Croaker et al. [2] is used to extract flow-induced noise sources from the flow and predict the propagation of the resulting pressure waves and their interaction with the airfoil.

2 Numerical Flow-Induced Noise Prediction

2.1 Hydrodynamic Data and Acoustic Sources

A wall-mounted airfoil with a NACA 0012 profile of reference chord length $c = 0.2$ m is considered. The airfoil has a rounded trailing edge with diameter of 0.003 m with a resulting chord length of 0.19 m. The airfoil has a span $s = 0.2$ m corresponding to an aspect ratio of 1 and was oriented at zero degree angle of attack relative to the incoming free stream velocity $U_\infty = 20$ m/s. This corresponds to a Mach number of 0.06 and a Reynolds number based on chord of 274,000. An LES of the unsteady flow field around the wall-mounted airfoil is performed by applying a filter to the incompressible Navier–Stokes equations and separating the hydrodynamic fluctuations into a component that can be resolved by the computational grid and a sub-grid scale component. The filtered incompressible Navier–Stokes equations are given by

$$\rho_f \frac{\partial \hat{u}_i}{\partial t} + \rho_f \frac{\partial}{\partial y_i}\left(\hat{u}_i \hat{u}_j\right) = -\frac{\partial \hat{p}}{\partial y_j} + 2\left(\mu_f + \mu_{\mathrm{SGS}}\right)\frac{\partial}{\partial y_j}\hat{S}_{ij} \tag{1}$$

$$\frac{\partial \hat{u}_j}{\partial y_j} = 0 \tag{2}$$

where $\hat{p}$ is the filtered pressure and $\hat{u}_i$ represents the components of the resolved velocity vector. μ_f and ρ_f are the viscosity and density of the fluid at rest. $\hat{S}_{ij}$ is the strain rate tensor of the resolved scales. The wall-adapting local eddy viscosity model of Nicoud and Ducros [8] is used to define the eddy viscosity, μ_{SGS}, which accounts for the influence of the sub-grid scales on the filtered motion.

A fully structured CFD model of the wall-mounted airfoil was created using a total of 88×10^6 hexahedral cells. The first cell height was placed within $y^+ \approx 0.5$ normalised wall units, and a fine mesh was used throughout the boundary layer and near-wake regions. The wall-mounted airfoil is located in a square tunnel with side length 0.93 m. The computational model extends 1.7 m upstream of the leading edge and 3.7 m downstream of the trailing edge. Figure 1 shows the computational model and associated mesh, whereby every second grid line is shown. Figure 1a shows an image of the airfoil surface and the surrounding tunnel floor. Figure 1b and c

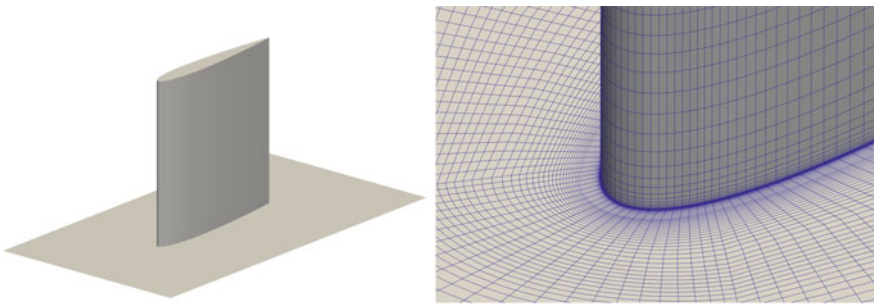

(a) Wall-mounted airfoil

(b) Mesh of junction leading edge

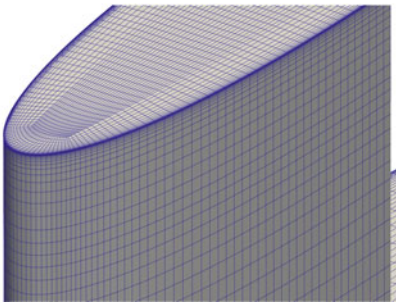

(c) Mesh of tip leading edge

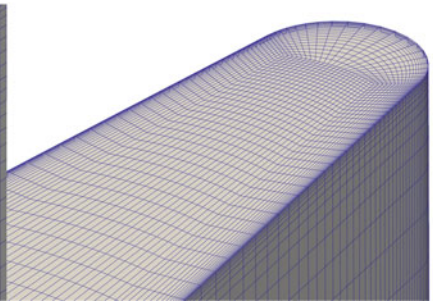

(d) Mesh of tip trailing edge

Fig. 1 CFD mesh for the wall-mounted airfoil, every second grid line shown

shows mesh details of the airfoil leading edge near the wall junction and airfoil tip, respectively. Figure 1d shows the mesh detail of the trailing edge of the airfoil tip.

The LES equations were solved using an iterative, segregated solution method with the pressure–velocity coupling handled using the pressure implicit with splitting of operator algorithm. A blended spatial differencing scheme was used with 95% second-order central differencing and 5% second-order upwind differencing. The blending of the upwind differencing adds numerical diffusion and increases the stability of the convection equation. A second-order backward implicit scheme was used for the temporal discretisation.

The transient simulation was executed with a time step size of 2×10^{-7} s and was allowed to progress until the flow field achieved quasi-periodicity. Recording of the acoustic source data then commenced with the entire flow field stored at intervals of 5×10^{-5} s. Lighthill [5] demonstrated that fluctuations in the stresses acting on a fluid generate pressure waves which travel to the far field as sound. For low Mach number flows, these Lighthill stresses are approximately equal to the Reynolds stress tensor and are given by $T_{ij} = \rho_f u_i u_j$, where u_i represents the components of the velocity vector. Time histories of these Lighthill stresses were extracted from the recorded hydrodynamic data and divided into equal segments with a length of 248 records and 50% overlap. A Hanning window function was applied to each segment of the Lighthill tensor time histories before converting them to frequency spectra.

2.2 Propagation of Flow-Induced Pressure Waves

The pressure waves generated by fluctuations in the Lighthill stress tensor propagate to the far field and are reflected, scattered and diffracted by a body in their path. The reflection, scattering and diffraction of the pressure waves by a body can be resolved using the boundary element method, provided that the pressure field incident on the body is known. Using a near-field formulation, the pressure on the body p_a^{inc} is given by Croaker et al. [1]

$$p_a^{\text{inc}} = \lim_{\epsilon \to 0} \int_{\Omega - V_\epsilon} T_{ij}\left(\mathbf{y}, \omega\right) \frac{\partial^2 G_h}{\partial y_i \partial y_j} dy \tag{3}$$

where y_i is the ith component of the flow-induced noise source position vector $\mathbf{y}$, Ω represents the computational domain, and V_ϵ is an exclusion neighbourhood taken around the point on the body $\mathbf{x}$ where the near-field pressure is computed. Singularities occur when $\mathbf{y} = \mathbf{x}$, and the exclusion neighbourhood is used to solve the resulting singular integrals using a semi-analytical technique [1]. The three-dimensional harmonic free-field Green's function is used to describe the propagation of the acoustic waves

$$G_h = \frac{e^{ik_a r}}{4\pi r} \tag{4}$$

where $i = \sqrt{-1}$, k_a is the acoustic wave number, and $r = |\mathbf{x} - \mathbf{y}|$.

The scattering by the body of the near-field incident pressure is solved using the inhomogeneous Helmholtz equation given by

$$\triangle p_a(x) + k_a^2 p_a = -Q \tag{5}$$

where $\triangle$ is the Laplacian operator and Q is the acoustic source. Equation (5) is combined with the near-field formulation for the pressure given by Eq. (3) and the hard-walled boundary condition on the surface of the airfoil $\frac{\partial p_a}{\partial n} = 0$ to calculate the scattered field on the wall-mounted airfoil as follows [6]:

$$c(\mathbf{y})\, p_a(\mathbf{y}) + \int_\Gamma p_a(\mathbf{x}) \frac{\partial G_h}{\partial n(\mathbf{x})} d\Gamma = p_a^{\text{inc}}(\mathbf{y}) \tag{6}$$

where n is the unit normal to the boundary. $c(\mathbf{y})$ is a free-term coefficient which equals 1 in the interior domain and 0.5 on a smooth boundary. Γ is the boundary of the domain.

In the current work, Eq. (6) is solved using a conventional boundary element method (BEM). Linear, discontinuous boundary elements were used to create the three-dimensional BEM model. The leading and trailing edges are discretised with a finer resolution mesh to ensure that interaction of the incident field with the geometry is accurately captured. A half-space Green's function was used to account for reflection of sound waves by the tunnel floor. The nodal points of the BEM elements also represent the locations used to calculate the incident pressure using Eq. (3). Once the scattered pressures on the airfoil have been determined, the total far-field pressure is then calculated.

3 Experimental Set-up

The measurements were conducted in the UNSW Acoustic Tunnel (UAT) which is an open-jet type facility. The UAT consists of a square open jet with a 0.455 m × 0.455 m cross section exhausting into a 3 m × 3.2 m × 2.15 m anechoic chamber treated on the inside with Melamine foam. All measurements in the present work were performed at a free stream velocity of 20 m/s with a free stream turbulence intensity, measured using a hotwire probe, of approximately 0.6%.

Two 6 mm thick, 300 mm long end plates were attached to the top and bottom edges of the test section inlet, and the airfoil was bolted to the bottom plate. The leading edge of the airfoil was positioned 30 mm downstream of the inlet. A coordinate

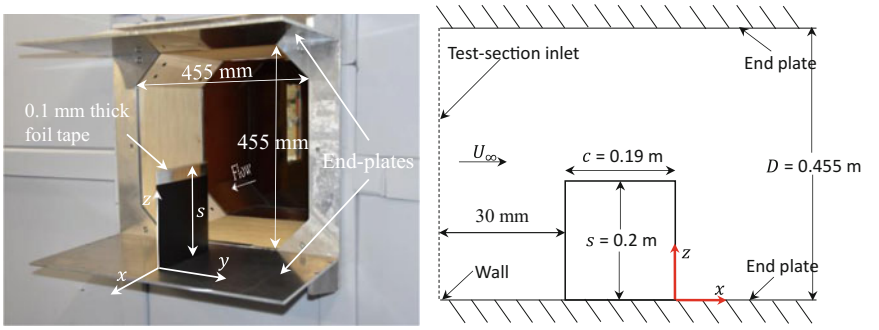

(a) Airfoil mounted in the test section of the UAT

(b) Schematic diagram showing the position of the airfoil in the tunnel

Fig. 2 Wall-mounted airfoil set-up in the UAT

system with origin at the trailing edge is shown in Fig. 2. The coordinate system was defined such that the streamwise coordinate x is positive in downstream direction, spanwise coordinate z is positive in the wall-normal direction, and y is the chord-normal coordinate. Figure 2 shows (a) the airfoil mounted in the UAT during the measurements and (b) a schematic view of the airfoil's location with respect to the wall and test section inlet.

A Dantec Dynamic 55P16 single-sensor constant temperature hotwire probe was used to measure the mean and fluctuating components of the streamwise velocity across the wake of the airfoil at a streamwise distance of $x/c = 0.025$ from the trailing edge and at spanwise locations $z/s = 0.5, 0.9$ and 0.975. The probe was mounted such that the sensor wire was parallel to the spanwise coordinate z and traversed through the wake on a Dantec Dynamic traverse which has a positional accuracy of $6\,\mu$m. The hotwire probe was connected to a Dantec Dynamic multichannel CTA 54N80, and the hotwire voltage was sampled at 51.2 kHz. The mean velocity and rms of hotwire velocity were obtained by averaging 10 records each with 8192 data points. For the spectral measurements, 50 records with 8192 data points were used. The auto-spectral densities were obtained by applying a Hanning window to each record before Fourier transforming and averaging them.

4 Hydrodynamic Results and Measurements

Figure 3 shows the flow structures present around the wall-mounted airfoil. Contour surfaces of constant Q-criterion were used to identify the main structures in the flow. The Q-criterion surfaces are coloured by the magnitude of the vorticity. Strong vortex structures are observed in the tip region. At the mid-span, a laminar boundary layer forms over the leading edge of the airfoil. This laminar boundary layer experiences break-up at approximately 60% of the chord and then transitions to turbulence over

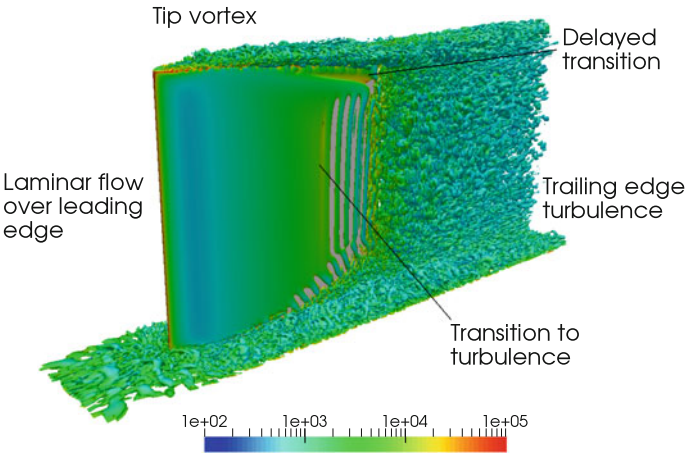

Fig. 3 Flow structures around the wall-mounted airfoil. Q-criterion iso surfaces coloured by the magnitude of the vorticity vector

the remainder of the chord. The generation of vortical structures is also observed at the airfoil–wall junction and within the wall boundary layer. At approximately 90% span close to the trailing edge, the strong pressure gradients induced by the tip vortices suppress the growth of the boundary layer and delay the break-up of the laminar boundary layer.

Figures 4, 5 and 6 compare the normalised mean velocity profile U/U_∞, normalised rms of the velocity fluctuations u'/U_∞ and velocity auto-spectral densities $G_{uu}(f)$ obtained from the numerical simulation with the measurements at 50%, 90% and 97.5% span, respectively. Figures 4f, 5f and 6f show the spanwise vorticity at an instant in time for the region near the trailing edge. The black line indicates the line over which the normalised mean and rms velocity profiles are recorded. The black dots positioned at $y/c = 0, 0.01$ and 0.02 represent the three locations at which the auto-spectral densities were recorded. The normalised mean velocity profiles predicted with the LES compare favourably with the measurements at all spanwise locations. The LES results are approximately symmetric about the mean chord line, with the minimum normalised velocity occurring at $y/c = 0$ at all spanwise locations. The measurements exhibit asymmetry, and the minimum normalised velocity occurs at a slight offset from $y/c = 0$. Uncertainty in hotwire positioning and the finite size of the sensor, which results in area averaging of the velocity fluctuations, is likely responsible for these quantitative discrepancies. Additionally, a single-sensor hotwire can be expected to have larger errors in a three-dimensional flow field due to its inability to resolve all three components of the velocity. Despite the observed discrepancies, there is good agreement between numerical results and measurements for the normalised mean velocity. The numerical normalised rms velocity profiles also show good agreement with the measurements. The magnitude and main features of the rms velocity fluctuations are well captured in the LES results.

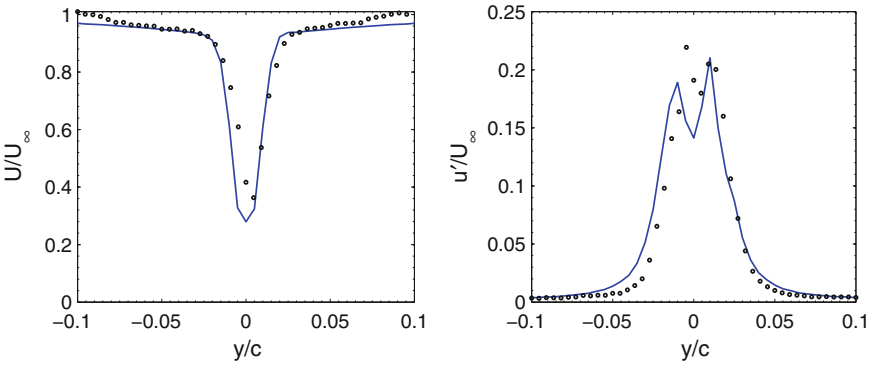

(a) Normalised mean velocity (b) Normalised rms velocity

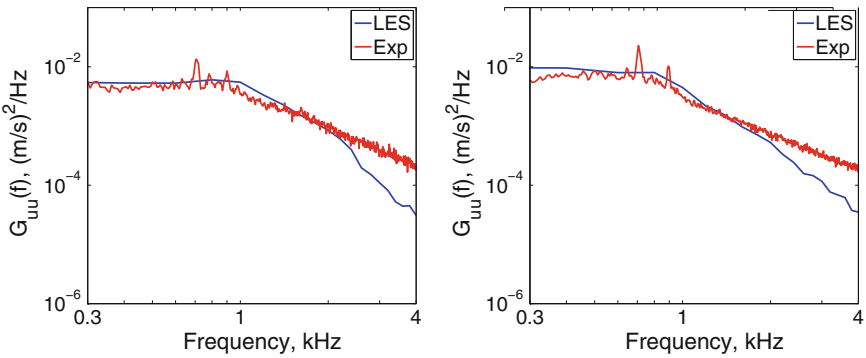

(c) Velocity autospectrum at $y/c = 0$ (d) Velocity autospectrum at $y/c = 0{\cdot}01$

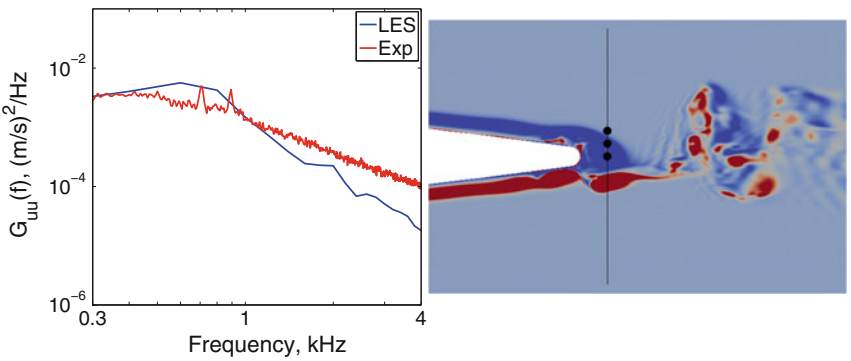

(e) Velocity autospectrum at $y/c = 0.02$ (f) Instantaneous spanwise vorticity

Fig. 4 Normalised mean and rms velocity profiles and auto-spectral densities at 50% of span. Results show comparison between LES (blue) and measurements (black). Spanwise vorticity plot shows measurement locations with the vorticity contours from -5000 to 5000 s^{-1}

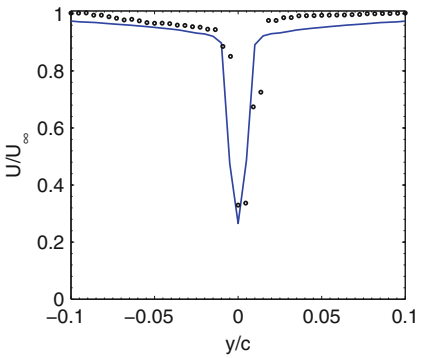

(a) Normalised mean velocity

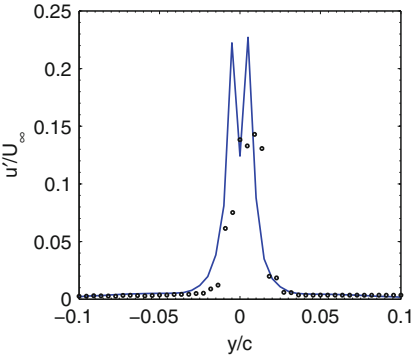

(b) Normalised rms velocity

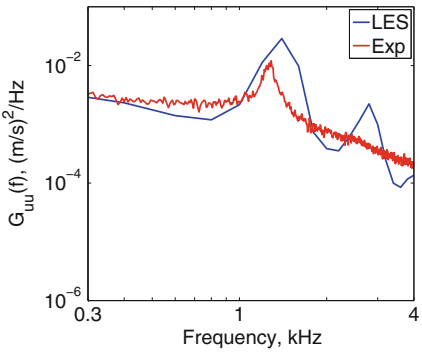

(c) Velocity autospectrum at $y/c = 0$

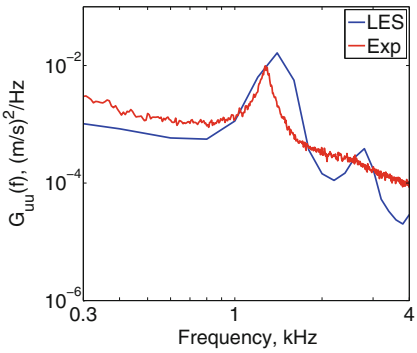

(d) Velocity autospectrum at $y/c = 0.01$

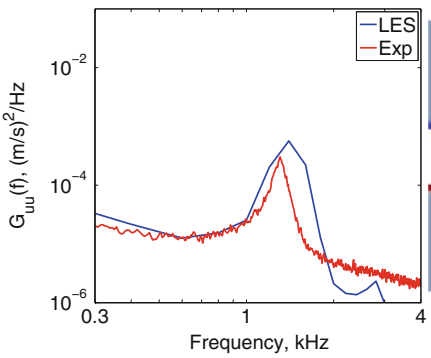

(e) Velocity autospectrum at $y/c = 0.02$

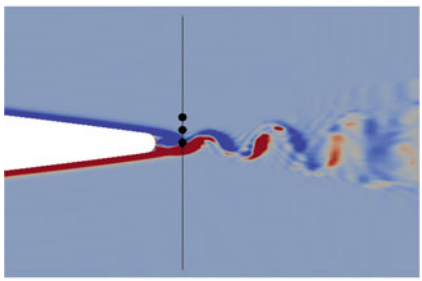

(f) Instantaneous spanwise vorticity

Fig. 5 Normalised mean and rms velocity profiles and auto-spectral densities at 90% of span. Results show comparison between LES (blue) and measurements (black). Spanwise vorticity plot shows measurement locations with the vorticity contours from -5000 to 5000 s^{-1}

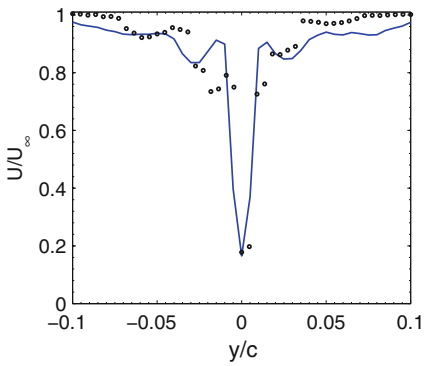

(a) Normalised mean velocity

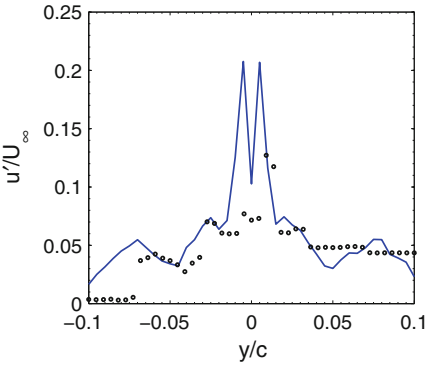

(b) Normalised rms velocity

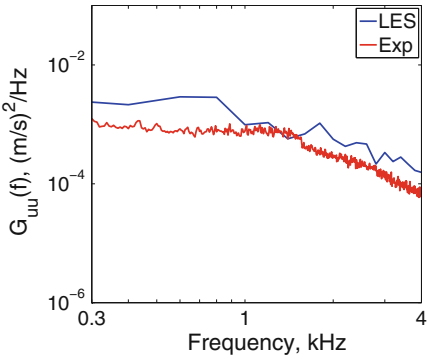

(c) Velocity autospectrum at $y/c = 0$

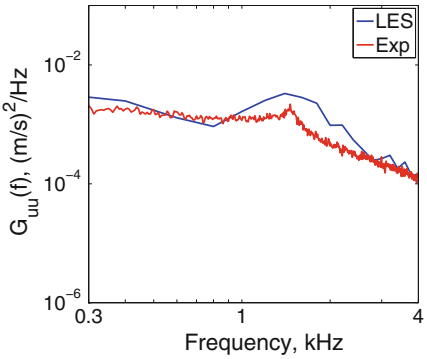

(d) Velocity autospectrum at $y/c = 0.01$

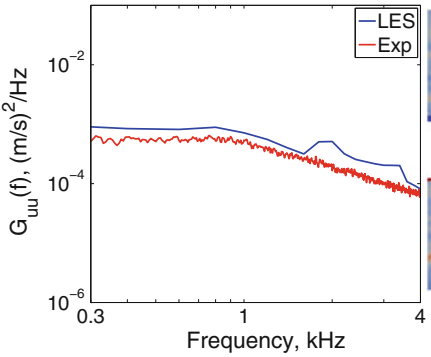

(e) Velocity autospectrum at $y/c = 0.02$

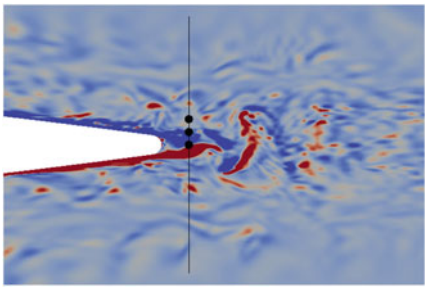

(f) Instantaneous spanwise vorticity

Fig. 6 Normalised mean and rms velocity profiles and auto-spectral densities at 97.5% of span. Results show comparison between LES (blue) and measurements (black). Spanwise vorticity plot shows measurement locations with the vorticity contours from -5000 to 5000 s^{-1}

Due to the asymmetry in the measured mean velocity profiles and the offset of the peak mean velocity from $y/c = 0$, the auto-spectral densities predicted from the LES data were averaged over a ± 1 mm range around the measurement point. Figure 4c and d shows that the auto-spectral densities at 50% span predicted with the LES data are in excellent agreement with the measurements at $y/c = 0$ and 0.01 for frequencies up to approximately 2 kHz. Beyond this frequency, the mesh resolution is no longer able to sufficiently resolve the velocity fluctuations and the energy decreases more rapidly than is observed in the measurements. For $y/c = 0.02$ in Fig. 4e, the auto-spectral density predicted with the LES contains more energy at lower frequencies than is observed in the measured data and the decrease in energy with frequency is slightly higher. However in general, there is good agreement between simulation results and measurements up to approximately 2 kHz.

Figure 5f shows the instantaneous spanwise vorticity of the flow at 90% span. The vorticity contours indicate that the flow is free of small-scale structures near the trailing edge of the airfoil and that laminar vortex shedding occurs downstream of the trailing edge. These vortices begin to break up into smaller scale structures as they travel further downstream. Figure 5c–e shows the velocity auto-spectral densities at 90% span for $y/c = 0$, 0.01 and 0.02, respectively. At all measurement locations, the broadened tone associated with the vortex shedding is well predicted with the LES; however, the peak level and shedding frequency are slightly over-predicted with the LES. The numerical results also capture a broadened tone at the second harmonic of the vortex-shedding frequency that is not present in the measured data. The reason for this discrepancy is under investigation. Both LES results and measured data show two orders of magnitude reduction in the auto-spectral density level at $y/c = 0.02$ compared to $y/c = 0.01$, which indicates that at this spanwise location the wake is very thin.

At 97.5% span, the flow in the vicinity of the trailing edge contains many small-scale flow features as shown in Fig. 6f. This is a combination of flow structures that develop in the boundary layer and flow structures from the tip vortices that travel past the trailing edge. Figure 6c–e shows the velocity auto-spectral densities at 97.5% span for $y/c = 0$, 0.01 and 0.02, respectively. The magnitude and extent of the broadband hump observed in the measured data at approximately 1.5 kHz at $y/c = 0.01$ are over-predicted with the LES; however, the overall levels and shape of the spectra agree favourably with measurements.

5 Far-Field Acoustic Predictions

Figure 7 shows the directivity of the far-field pressure magnitude in the plane of the airfoil tip on a 1 m arc about the centre of the airfoil chord, from 450 Hz to 1.65 kHz in 400 Hz increments. At the lower frequencies corresponding to 450 and 850 Hz, the maximum far-field pressure is oriented towards the positive streamwise axis. This indicates that at these frequencies, the far-field pressure is dominated by turbulence interaction with the leading edge at the junction and tip of the airfoil. This

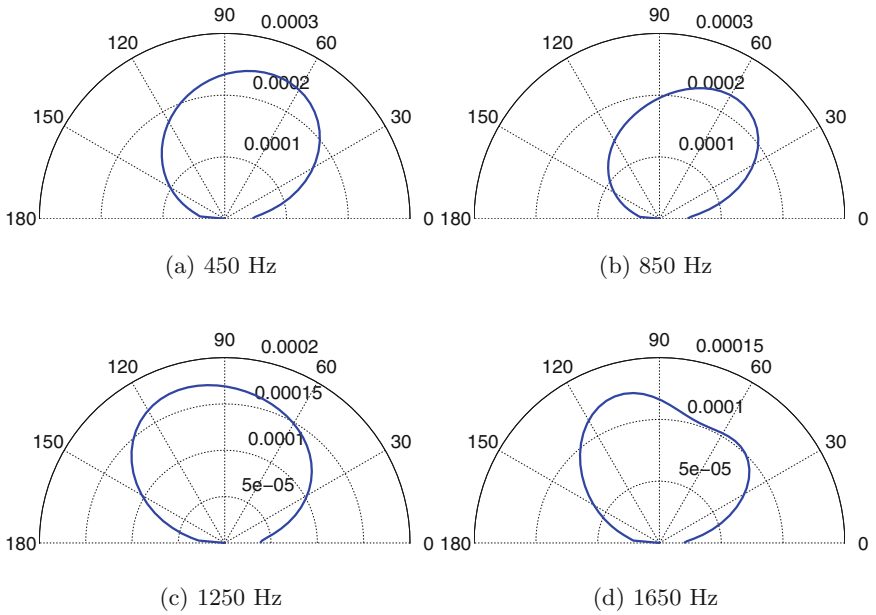

(a) 450 Hz (b) 850 Hz

(c) 1250 Hz (d) 1650 Hz

Fig. 7 Directivity of the far-field sound pressure level in at a distance 1 m from the centre of the airfoil chord calculated in the plane of the airfoil tip

result is consistent with the experimental findings of Moreau et al. [7]. At the higher frequencies corresponding to 1.25 and 1.65 kHz, the maximum far-field pressure is oriented upstream of the leading edge. This suggests that at these frequencies, trailing edge noise and blunt vortex-shedding noise are the dominant flow-induced noise mechanisms. Similar observations were made from the measurements of Moreau et al. [7]. The directivity at 1.65 kHz shows the formation of a secondary lobe due to backscattering of the acoustic pressure by the leading edge of the airfoil. This occurs as the chord length of the airfoil becomes comparable to the acoustic wavelength at this frequency and the airfoil is no longer acoustically compact.

Figure 8 shows the power spectral density of the acoustic pressure predicted at a distance of 1 m from the centre of the airfoil chord at the airfoil tip height and normal to the mean chord line. The low-frequency component of the noise, attributed to turbulence interaction with the leading edge of the airfoil, is of comparable magnitude to the high-frequency component which is attributed to trailing edge noise mechanisms. A similar trend was observed by Moreau et al. [7], although the airfoil in that study had a larger chord length and was subjected to higher Reynolds numbers.

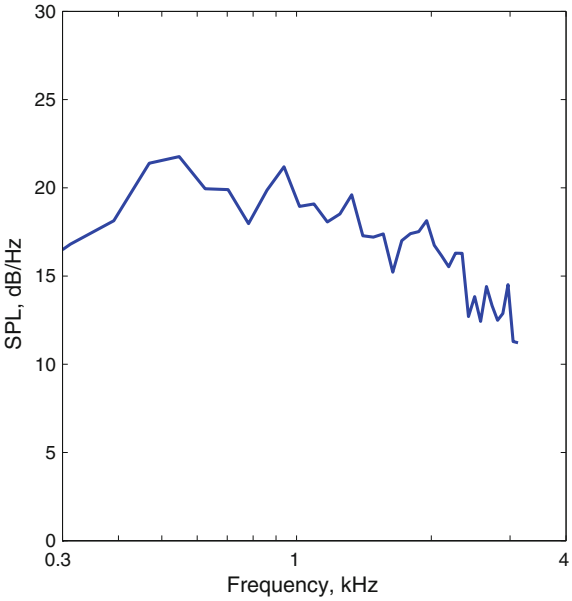

Fig. 8 PSD of the far-field sound 1 m from the centre of the airfoil chord and normal to the mean chord line

6 Summary

The flow field around a wall-mounted airfoil at a Reynolds number Re_c = 274,000 and Mach number $M = 0.06$ has been numerically predicted and experimentally measured. The numerical results obtained from an LES model are in good agreement with the measurements. A hybrid CFD-BEM technique was then used to predict the flow-induced noise produced by the wall-mounted airfoil. The directivity of the far-field sound reveals that the lower frequency noise is dominated by interaction of turbulent pressure fluctuations with the leading edge. At higher frequencies, trailing edge noise mechanisms dominate the far-field sound. Future work will focus on experimental validation of the far-field sound predicted with the hybrid CFD-BEM technique.

References

1. Croaker, P., Kessissoglou, N., Marburg, S.: Strongly singular and hypersingular integrals for aeroacoustic incident fields. Int. J. Num. Methods Fluids **77**, 274–318 (2015)
2. Croaker, P., Kessissoglou, N., Marburg, S.: Aeroacoustic scattering using a particle accelerated computational fluid dynamics/boundary element technique. AIAA J. **54**(7), 2116–2133 (2016)
3. Devenport, W.J., Simpson, R.L.: Time-dependent and time-averaged turbulence structure near the nose of a wing-body junction. J. Fluid Mech. **210**(1), 23–55 (1990)
4. Giuni, M., Green, R.B.: Vortex formation of squared and rounded tip. Aerosp. Sci. Technol. **29**(1), 191–199 (2013)

5. Lighthill, M.J.: On sound generated aerodynamically, I. General theory. Proc. R. Soc. A **211**, 564–587 (1952)
6. Marburg, S., Nolte, B. (eds.): Computational Acoustics of Noise Propagation in Fluids. Springer, Berlin, Germany (2008)
7. Moreau, D.J., Doolan, C.J., Alexander, W.N., Meyers, T.W., Devenport, W.J.: Wall-mounted finite airfoil-noise production and prediction. AIAA J. **54**(5), 1637–1651 (2016)
8. Nicoud, F., Ducros, F.: Subgrid-scale stress modelling based on the square of the velocity gradient tensor. Flow Turbul. Combust. **62**(3), 183–200 (1999)
9. Olcmen, S.M., Simpson, R.L.: Some features of a turbulent wing-body junction vortical flow. Int. J. Heat Fluid Flow **27**(6), 980–993 (2006)
10. Simpson, R.L.: Junction flows. Ann. Rev. Fluid Mech. **33**(1), 415–443 (2001)